# Pure and Applied Geophysics



# Robust Computations of Runup in Inclined U- and V-Shaped Bays

HARRISON HARTLE, <sup>1</sup> ALEXEI RYBKIN, <sup>1</sup> EFIM PELINOVSKY, <sup>2,3</sup> and DMITRY NICOLSKY <sup>4,5</sup>

Abstract—We present an exact analytical solution for computations of runup in constantly inclined U- and V-shaped bays. The provided solution avoids integration of indefinite double integrals in (Rybkin et al., Water Waves 3(1):267–296, 2021) and is based on a simple analytic expression for the Green's function. We analyze wave runup in parabolic and certain V-shaped bays, for which a particularly wide class of solutions are determinable analytically and for which a robust computational algorithm could be developed. Our results are effective in the context of narrow bays, where a generalized form of the Carrier-Greenspan transformation has been developed.

**Keywords:** Long wave runup, shallow water equations, Carrier-Greenspan transform, Green's function.

#### 1. Introduction

Tsunamis have been threatening coastal communities for centuries. One the main challenges in the tsunami hazard mitigation is obtaining an accurate and quick prediction of the tsunami runup at the shore. Having this information at hand and promptly can save numerous lives of coastal residents and visitors (Bernard & Titov, 2015). In Alaska and British Columbia, before arriving to the community's waterfront, a tsunami typically propagates through a network of channels and fjords. Analyzing tsunamis at the entrance can be used for developing of special

Published online: 20 October 2021

robust computations of runup heights and estimates of tsunami risk for communities at the head of bays.

Several empirical and numerical methods have been proposed for computations of the tsunami runup and the literature here is very extensive. At the same time, many analytical solutions have been proposed to compute the runup for constantly sloping plane beaches based on the well-known Carrier-Greenspan (CG) transform Carrier and Greenspan (1958), which cast the nonlinear shallow-water equations (SWEs) into a linear form with use of the hodograph transform. The CG transform was generalized to the case of constantly slopping bays (Rybkin et al., 2014) and a comparison with the numerical results revealed that this transformation work even in the double headed fjords (Raz et al., 2018).

Analytic and semi-analytic solutions of the nonlinear SWEs for a plane beach are given usually for initial disturbances with zero fluid velocity; see for example papers (Pedersen & Gjevik, 1983; Synolakis & Deb, 1988; Synolakis, 1991; Pelinovsky & Mazova, 1992; Tinti & Tonini, 2005; Antuono & Brocchini, 2007; Didenkulova et al., 2007, 2009; Madsen & Fuhrman, 2008; Didenkulova, 2009; Antuono & Brocchini, 2010; Dobrokhotov et al., 2010; Dobrokhotov & Tirozzi, 2010; Madsen & Schäffer, 2010; Dobrokhotov et al., 2013; Chugunov et al., 2020), where the tsunami wave runup on plane beached is analyzed. Similar analytical solutions for tsunami wave runup in narrow bays have been also derived and to lesser extent in narrow bays (Zahibo et al., 2006; Didenkulova & Pelinovsky, 2009; Rybkin et al., 2014; Harris et al., 2016; Garashin et al., 2016; Shimozono, 2016, 2020, 2021).

It is important to note that papers cited above use the initial disturbances only as water surface displacement with no fluid velocity. A few studies have considered nonzero initial velocities (Carrier et al.,

Department of Mathematics and Statistics, University of Alaska Fairbanks, Alaska 99775, USA.

<sup>&</sup>lt;sup>2</sup> Higher School of Economics, National Research University, Nizhny Novgorod, Russia.

Institute of Applied Physics, Nizhny Novgorod, Russia.

Geophysical Institute, University of Alaska Fairbanks, Alaska 99775, USA. E-mail: djnicolsky@alaska.edu

Saint Petersburg Electrotechnical University "LETI", 197376 St. Petersburg, Russia.

2003; Kânoğlu & Synolakis, 2006; Aydin & Kânoğlu, 2017; Nicolsky et al., 2018). It is important to note that one of the complications with a non-zero velocities is that the initial conditions in (x, t = 0) line and not mapped to hodograph variables  $(\sigma, \lambda = 0)$ , but rather on a manifold in the  $(\sigma, \lambda)$  coordinates. Recent works on providing appropriate initial and boundary conditions the  $(\sigma, \lambda)$  space help to overcome these complications (Rybkin, 2019; Rybkin et al., 2021).

In many above-mentioned manuscripts, analytical solutions are based on the Bessel or Bessel-Hankel transforms and require a computation of indefinite double integrals with Bessel functions. In particular, one has to map a function into the image space and then pull back, while ensuring an accuracy control over all calculations. For computing runup at the plane beaches, Carrier et al. (2003) and later Kânoğlu and Synolakis (2006) introduced a Green's function alternative, which avoid the above-mentioned computational challenges. In these works, using certain physically based assumptions, both non-zero initial conditions are transformed onto the line  $\lambda = 0$  and then integrated over with the Green's function. The latter has a finite support and could be easily computable, though not in terms of elementary functions. Finally Nicolsky et al. (2018); Rybkin (2019); Rybkin et al. (2021) used a Taylor formula to extend the initial conditions from the curve  $\lambda = \lambda_0(\sigma)$  to the line  $\lambda = 0$  with an arbitrary degree of accuracy both for plane and U-shaped bays. However, the double integration over the Bessel functions is still present in (Nicolsky et al., 2018; Rybkin et al., 2021).

Herein, we follow Carrier et al. (2003) and generalize this work in case of the U-shaped and V-shaped bays. In particular, we derive a Green's function (in terms of the Legendre functions) for runup problems and hence simplify the double integral computations commonly occurring in previous works. The outline of our paper is as follows: In Sect. 2, we discuss necessary background information and notation, including a general description of the shallow-water equations, Carrier-Greenspan transform, and specific details regarding the context of U-shaped and V-shaped bays. In Sect. 3, we consider the initial-value problem in  $(\sigma, \lambda)$ -space and derive a Green's function for arbitrary initial

conditions on  $(\sigma,0)$ . In Sect. 4, the Green's function is evaluated explicitly for 2/(2k+1)-power bays, yielding analytic solutions. The runup of a Gaussian wave and leading depression N-wave are analyzed in Sect. 5. Finally, Sect. 6 is devoted to additional discussion and concluding remarks.

#### 2. Background Information

In this article, we consider the behavior of waves in bays with cross section shown in Fig. 1. Cross-sectionally averaging the 2-D SWEs for a given bay cross-section S(H), assumed to functionally depend on only the total water height H(x, t), yields the associated 1-D system (Stoker, 1957; Johnson, 1997). Our initial-value problem in (x, t) coordinates, posed on  $(x, t) \in (-\infty, \infty) \times (0, \infty)$ , is then:

$$S_t + (Su)_x = 0, \quad u_t + uu_x + gH_x = gh_x,$$
 (1)

for a given resting water depth h=h(x) and initial conditions (ICs) specified by  $u_0(x)=u(x,0)$  and  $\eta_0(x)=\eta(x,0)$ ; the physical meanings of  $\eta(x,t)$  and u(x,t) are respectively the water height displacement from equilibrium along the central axis of the bay (hence  $\eta(x,t)=H(x,t)-h(x)$ ), and the cross-sectionally averaged longitudinal flow velocity. For our studies,  $h(x)=-\alpha x$  is taken as a linear function of slope  $\alpha$ , representing an infinitely long inclined channel with steepness  $h_x\equiv -\alpha$ .

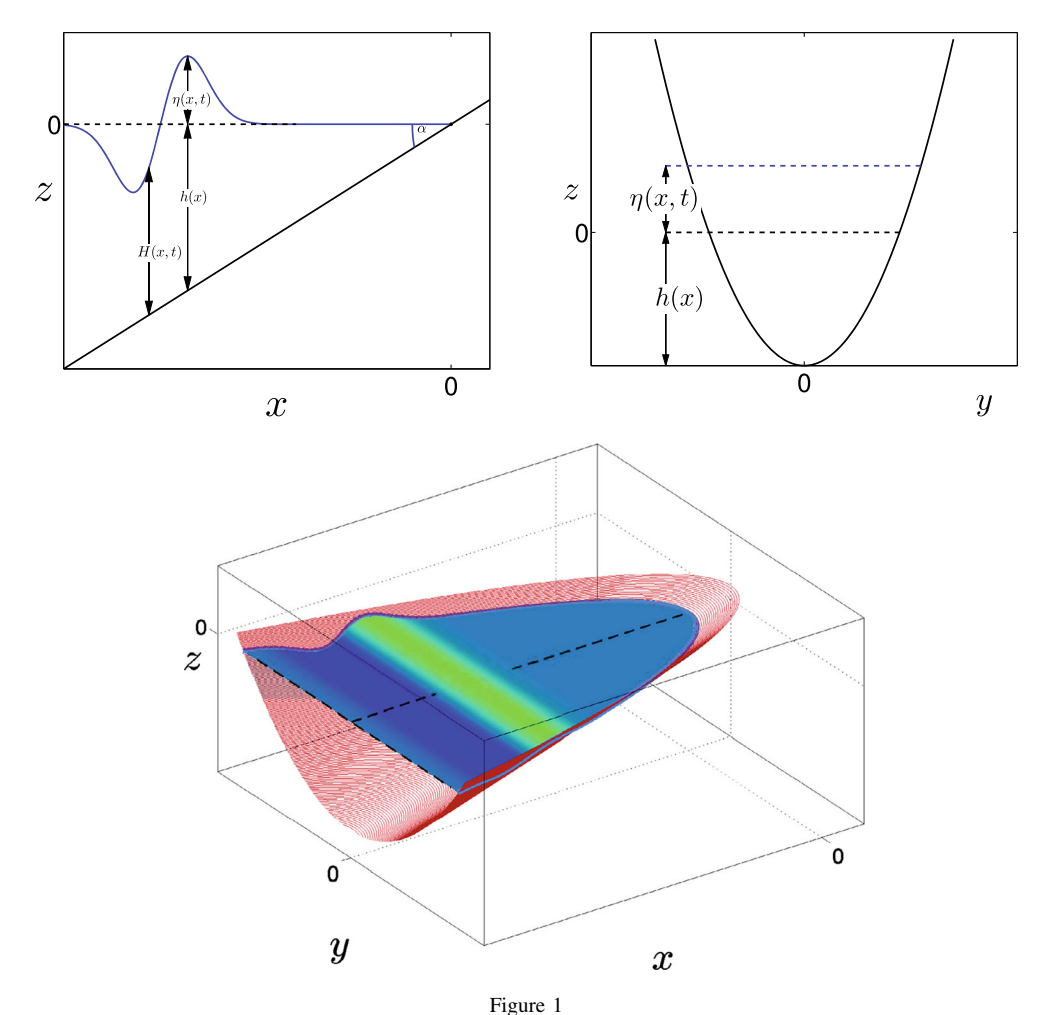
*U*-shaped and *V*-shaped bays are our primary bathymetries of interest. For such bays, the transverse geometry is of the form  $|y|^m$  for the real parameter  $m \ge 0$ , and bay cross-section function  $S = S(H) = \frac{m}{m+1} H^{1+\frac{1}{m}}$ . In this instance the 1-D shallow water equation (1) reduce to (Rybkin et al., 2014),

$$H_t + uH_x + m(m+1)^{-1}Hu_x = 0,$$
  
 $u_t + uu_x + gH_x = -g\alpha,$  (2)

which transform into a second-order hyperbolic PDE in  $(\sigma, \lambda)$  coordinates:

$$\Phi_{\lambda\lambda}(\sigma,\lambda) - \Phi_{\sigma\sigma}(\sigma,\lambda) - \frac{m+2}{m\sigma}\Phi_{\sigma}(\sigma,\lambda) = 0, \quad (3)$$

via a Carrier-Greenspan transform expressing  $\eta$ , u, x, and t as scalar fields on the hodograph plane  $(\sigma, \lambda)$  by



Bathymetry of a *U*-shaped bay. The upper left panel illustrates the geometric meaning of  $\eta$ , h, and H,  $\alpha$  and coordinates  $z = |y|^m + \alpha x$  and x; the upper right panel illustrates the transverse geometry of the bay; the lower panel gives a three-dimensional view of the same configuration

$$u(\sigma,\lambda) = \frac{m+1}{m} \sigma^{-1} \Phi_{\sigma}(\sigma,\lambda),$$

$$\eta(\sigma,\lambda) = \frac{1}{2g} \Phi_{\lambda}(\sigma,\lambda) - \frac{1}{2g} u(\sigma,\lambda)^{2},$$

$$x(\sigma,\lambda) = -\frac{1}{4\alpha g} \frac{m}{m+1} \sigma^{2} + \frac{1}{\alpha} \eta(\sigma,\lambda),$$

$$t(\sigma,\lambda) = \frac{1}{\alpha g} (\lambda - u(\sigma,\lambda)).$$
(4)

It is evident that all physical quantities as functions of  $(\sigma, \lambda)$  are fully determined from the potential function  $\Phi(\sigma, \lambda)$  by the above transformations. From those four fields we may obtain  $\eta(x, t)$  and u(x, t) by associating  $\eta(\sigma, \lambda)$  and  $u(\sigma, \lambda)$  with spacetime point  $(x(\sigma, \lambda), t(\sigma, \lambda))$ .

A general solution to the runup problem in parabolic  $(z=y^2)$  bays was found by Didenkulova and Pelinovsky (2011a) for  $u_0(\sigma)=0$ . As a general property, it was stated that parabolic-bay solutions must adopt the form  $(g(\lambda+\sigma)-g(\lambda-\sigma))/\sigma$  for some function  $\sigma$ . Further, an initial-value problem for infinite length V-shaped and U-shaped bays on  $(0,\infty)$  was solved for arbitrary  $\eta_0(x)$  recently (Garashin et al., 2016), although with the constraint of  $u_0(x)=0$  imposed. In the general case of arbitrary cross-section function S(H), no general solution has been obtained (Rybkin et al., 2014). At the same time, for the U- and V-shaped bays, the solution involves evaluating double integrals (Nicolsky et al., 2018; Rybkin et al., 2021).

The runup problem was solved by Carrier et al. (2003) for the plane-beach case with arbitrary initial  $\Phi(\sigma,0)$  and  $\Phi_{\lambda}(\sigma,0)$ . The authors obtained a Green's function representation and implemented it via numerical integration. We will follow Carrier et al. (2003) and generalize the solution to the V- and U-shaped bays with a Fourier-Bessel type transform, deriving a Green's function.

# 3. Solution for U-Shaped and V-Shaped Bays

In this section, a 1/m-th order Hankel-like transform is applied to the initial-value problem in  $(\sigma, \lambda)$  for infinite-length U-shaped bays. Initial data is specified along  $\lambda_0(\sigma)=0$  in the hodograph plane. The inverse Hankel-like transform leads to an expression for the Green's function, for the case of arbitrary  $\Phi(\sigma,0)$  and  $\Phi_{\lambda}(\sigma,0)$ . This results is a generalization of previous works (Carrier et al., 2003; Garashin et al., 2016).

Following Garashin et al. (2016), we define  $\Omega(s,\lambda)$  as the 1/m-th order Hankel transform of  $\sigma^{1/m}\Phi(\sigma,\lambda)$ :

$$\Omega(s,\lambda) = \int_0^\infty \sigma^{\frac{1}{m}+1} J_{\frac{1}{m}}(\sigma s) \Phi(\sigma,\lambda) d\sigma. \tag{5}$$

Upon multiplication of Eq. (3) through by  $\sigma^{1/m+1}J_{1/m}(\sigma s)$ , integration with respect to  $\sigma$  from 0 to  $\infty$ , we find that  $\Omega(s,\lambda)$  behaves as

$$\Omega_{\lambda\lambda} + s^2 \Omega = 0, \tag{6}$$

from which we trivially obtain a solution of the form:

$$\Omega(s,\lambda) = a(s)\cos(s\lambda) + b(s)\sin(s\lambda) \tag{7}$$

We apply arbitrary initial conditions in  $(\sigma, \lambda)$  space of the form  $\Phi(\sigma, 0) = p(\sigma)$  and  $\Phi_{\lambda}(\sigma, 0) = f(\sigma)$ , which are transformed via Eq. (5) into  $\Omega(s, 0) = \bar{p}(s)$  and  $\Omega_{\lambda}(s, 0) = \bar{f}(s)$ , respectively. Evaluating (7) at  $\lambda = 0$  gives  $a(s) = \bar{p}(s)$  and  $sb(s) = \bar{f}(s)$ , yielding the solution in terms of  $(s, \lambda)$  variables:

$$\Omega(s,\lambda) = \bar{p}(s)\cos(s\lambda) + s^{-1}\bar{f}(s)\sin(s\lambda). \tag{8}$$

We determine  $\Phi(\sigma, \lambda)$  through the inverse operation of our Hankel-type transform (5), from which we derive

$$\Phi(\sigma,\lambda) = \sigma^{-\frac{1}{m}} \int_{0}^{\infty} s J_{\frac{1}{m}}(\sigma s) \{\bar{p}(s)\cos(s\lambda) + s^{-1}\bar{f}(s)\sin(s\lambda)\} ds.$$
(9)

Expanding the terms  $\bar{p}(s)$  and  $\bar{f}(s)$  into their full integral expressions, separating into two integrals and utilizing column-vector notation in light of the similarity of the two terms, we get

$$\Phi(\sigma,\lambda) = \int_{0}^{\infty} \frac{J_{\frac{1}{m}}(\sigma s)}{\sigma_{m}^{\frac{1}{m}}} \times \left[ \left( \frac{s \cos(s\lambda)}{\sin(s\lambda)} \right) \cdot \int_{0}^{\infty} \left( \frac{p(\psi)}{f(\psi)} \right) \right. \\
\left. \psi^{1+\frac{1}{m}} J_{\frac{1}{m}}(\psi s) d\psi \right] ds = \int_{0}^{\infty} \frac{J_{\frac{1}{m}}(\sigma s)}{\sigma_{m}^{\frac{1}{m}}} \left( \frac{\partial_{\lambda}}{1} \right) \cdot \left. \left[ \sin(s\lambda) \int_{0}^{\infty} \left( \frac{p(\psi)}{f(\psi)} \right) \psi^{1+\frac{1}{m}} J_{\frac{1}{m}}(\psi s) d\psi \right] ds$$

Further, by expressing  $p(\psi)$  and  $p(\psi)$  as integrals of  $\delta$ -functions with respect to a new variable  $\xi$  (along-side slight algebraic rearrangement, in the interest of space), we compute

$$\begin{split} \varPhi(\sigma,\lambda) &= \int_0^\infty \frac{J_{\frac{1}{m}}(\sigma s)}{\sigma^{\frac{1}{m}}} \begin{pmatrix} \hat{\mathbf{o}}_{\lambda} \\ 1 \end{pmatrix} \cdot \\ &\cdot \left[ \sin(s\lambda) \int_0^\infty \left( \int_0^\infty \binom{p(\xi)}{f(\xi)} \right) \delta(\xi - \psi) d\xi \right) \\ &\frac{J_{\frac{1}{m}}(\psi s)}{\psi^{-1 - \frac{1}{m}}} d\psi \right] ds. \end{split}$$

We may rearrange the functions  $p(\xi)$  and  $f(\xi)$  out from under the integrals with respect to  $\psi$  and s, as long as they remain under the  $\xi$ -integral. We do so by exchanging integration order from  $\xi$ ,  $\psi$ , s to  $\psi$ , s,  $\xi$ , resulting in:

$$\begin{split} \varPhi(\sigma,\lambda) &= \int\limits_0^\infty \binom{p(\xi)}{f(\xi)} \cdot \binom{\widehat{o}_\lambda}{1} \\ &\left\{ \int\limits_0^\infty \left[ \int\limits_0^\infty \frac{J_{\frac{1}{m}}(\psi s) \delta(\xi-\psi) d\psi}{\psi^{-1-\frac{1}{m}}} \right] \right. \\ &\left. \frac{J_{\frac{1}{m}}(\sigma s) \sin(s\lambda) ds}{\sigma_m^{\frac{1}{m}}} \right\} d\xi. \end{split}$$

Evaluating the innermost integral (with integration variable  $\psi$ ), and rearranging further, we obtain

$$\Phi(\sigma,\lambda) = \int_{0}^{\infty} {p(\xi) \choose f(\xi)} \cdot {\partial_{\lambda} \choose 1} \\
\left\{ \frac{\xi^{1+\frac{1}{m}}}{\sigma_{m}^{\frac{1}{m}}} \int_{0}^{\infty} J_{\frac{1}{m}}(\sigma s) J_{\frac{1}{m}}(\xi s) \sin(s\lambda) ds \right\} d\xi. \tag{10}$$

The Green's function  $G^{(m)}(\sigma, \lambda; \xi)$  is then defined as what is within the braces in the above expression, or equivalently

$$\Phi(\sigma,\lambda) = \int_{0}^{\infty} p(\xi)G_{\lambda}^{(m)}(\sigma,\lambda;\xi)d\xi 
+ \int_{0}^{\infty} f(\xi)G^{(m)}(\sigma,\lambda;\xi)d\xi.$$
(11)

The integral in (10) is evaluated by comparison with formula (6.672.1) of Gradshteyn and Ryzhik (1996), the result of which is

where  $P_{\nu}$  is the  $\nu$ -th degree Legendre function of the

As  $m \to \infty$ , we have  $G^{(\infty)}(\sigma, \lambda; \xi) = \xi \int_0^\infty J_0(\sigma s) J_0(\xi s) \sin(s\lambda) ds$ , which is the Green's function for a planar beach Carrier et al. (2003) and Kânoğlu and Synolakis (2006). It was shown by Carrier et al. (2003) to be expressible in terms of complete elliptic integrals of the first kind, a representation usable for computationally efficient numerical solutions. This limit can be seen straightforwardly from the intermediate form

$$G^{(m)}(\sigma,\lambda;\xi) = \sigma^{-\frac{1}{m}} \xi^{1+\frac{1}{m}} \int\limits_0^\infty J_{\frac{1}{m}}(\sigma s) J_{\frac{1}{m}}(\xi s) \sin(s\lambda) ds,$$

a precursor to (12).

4. Solution for 
$$m = 2/(2k+1)$$
 bays

In this section, we consider a particular case of bays, the bathymetry of which is associated with m=2/(2k+1), where k is a non-negative integer. A parabolically shaped bay is described by k=0, while k=1,2,... relate to V-shaped bay bathymetries. In these cases, we have  $\pi/m=k\pi+\pi/2$ , and hence the Green's function, given by (12) simplifies to

$$\begin{split} G^{(2/(2k+1))}(\sigma,\lambda;\xi) &= \frac{1}{2} \left(\frac{\xi}{\sigma}\right)^{1+k} \\ &\left\{ P_k \left(\frac{\sigma^2 + \xi^2 - \lambda^2}{2\sigma\xi}\right), \quad |\sigma - \xi| < \lambda < \sigma + \xi \\ 0, \quad & \text{otherwise} \end{split} \right.. \end{split}$$

The Legendre function  $P_k$  for a nonnegative integer k becomes the Legendre polynomial of the degree k.

$$G^{(m)}(\sigma,\lambda;\xi) \equiv \left(\frac{\xi}{\sigma}\right)^{\frac{1}{m}+\frac{1}{2}} \begin{cases} -\frac{1}{\pi}\cos\left(\frac{\pi}{m}\right)Q_{\frac{1}{m}-\frac{1}{2}}\left(-\frac{\sigma^2+\xi^2-\lambda^2}{2\sigma\xi}\right), & \sigma+\xi<\lambda\\ & \frac{1}{2}P_{\frac{1}{m}-\frac{1}{2}}\left(\frac{\sigma^2+\xi^2-\lambda^2}{2\sigma\xi}\right), & |\sigma-\xi|<\lambda<\sigma+\xi, \\ & 0, & 0<\lambda<|\sigma-\xi| \end{cases}$$
(12)

first kind, and  $Q_v$  is the v-th degree Legendre function of the second kind. Plots of Green functions  $G^{(m)}(\sigma, \lambda; \xi)$  for various values of m are shown in Fig. 2.

Furthermore, it is easy to note that  $|\sigma - \xi| < \lambda < \sigma + \xi$  is equivalent to  $|\sigma - \lambda| < \xi < \sigma + \lambda$ , and we thus obtain

$$\begin{split} G^{(2/(2k+1))}(\sigma,\lambda;\xi) &= \\ \begin{cases} g^{(k)}(\sigma,\lambda;\xi), & |\sigma-\lambda| < \xi < \sigma + \lambda \\ 0, & \text{otherwise} \end{cases}, \end{split}$$

where

$$g^{(k)}(\sigma,\lambda;\xi) = \frac{1}{2} \left(\frac{\xi}{\sigma}\right)^{1+k} P_k \left(\frac{\sigma^2 + \xi^2 - \lambda^2}{2\sigma\xi}\right).$$

Consequently, the potential  $\Phi(\sigma, \lambda)$  is expressed by

$$\begin{split} \varPhi(\sigma,\lambda) &= \frac{\partial}{\partial \lambda} \int_{|\sigma-\lambda|}^{\sigma+\lambda} p(\xi) g^{(k)}(\sigma,\lambda;\xi) d\xi \\ &+ \int_{|\sigma-\lambda|}^{\sigma+\lambda} f(\xi) g^{(k)}(\sigma,\lambda;\xi) d\xi \\ &= \int_{|\sigma-\lambda|}^{\sigma+\lambda} \left( p(\xi) g_{\lambda}^{(k)}(\sigma,\lambda;\xi) \right. \\ &+ f(\xi) g^{(k)}(\sigma,\lambda;\xi) \right) d\xi \\ &+ p(\sigma+\lambda) g^{(k)}(\sigma,\lambda;\sigma+\lambda) \\ &- p(|\sigma-\lambda|) g^{(k)}(\sigma,\lambda;|\sigma-\lambda|) sign(\lambda-\sigma). \end{split}$$

After considering cases  $\lambda < \sigma$  and  $\lambda > \sigma$ , it is possible to show that

$$\Phi(\sigma,\lambda) = \frac{1}{2} \frac{1}{\sigma^{k+1}} \int_{|\sigma-\lambda|}^{\sigma+\lambda} f(\xi) \xi^{k+1} P_k \left( \frac{\sigma^2 + \xi^2 - \lambda^2}{2\sigma \xi} \right) d\xi 
- \frac{1}{2} \frac{\lambda}{\sigma^{k+2}} \int_{|\sigma-\lambda|}^{\sigma+\lambda} p(\xi) \xi^k P_k' \left( \frac{\sigma^2 + \xi^2 - \lambda^2}{2\sigma \xi} \right) d\xi 
+ \frac{1}{2} \left( \frac{\sigma + \lambda}{\sigma} \right)^{k+1} p(\sigma + \lambda) 
+ \frac{1}{2} \left( \frac{\sigma - \lambda}{\sigma} \right)^{k+1} p(|\sigma - \lambda|).$$
(13)

In case of the parabolic bays, k=0,  $P_0=1$  and  $P_0'=0$ , and consequently the potential  $\Phi$  simplifies to

$$\Phi(\sigma,\lambda) = \frac{1}{2\sigma} [(\sigma + \lambda)p(\sigma + \lambda) + (\sigma - \lambda)p(|\sigma - \lambda|) + \int_{|\sigma - \lambda|}^{(\sigma + \lambda)} f(\xi)\xi d\xi \right].$$
(14)

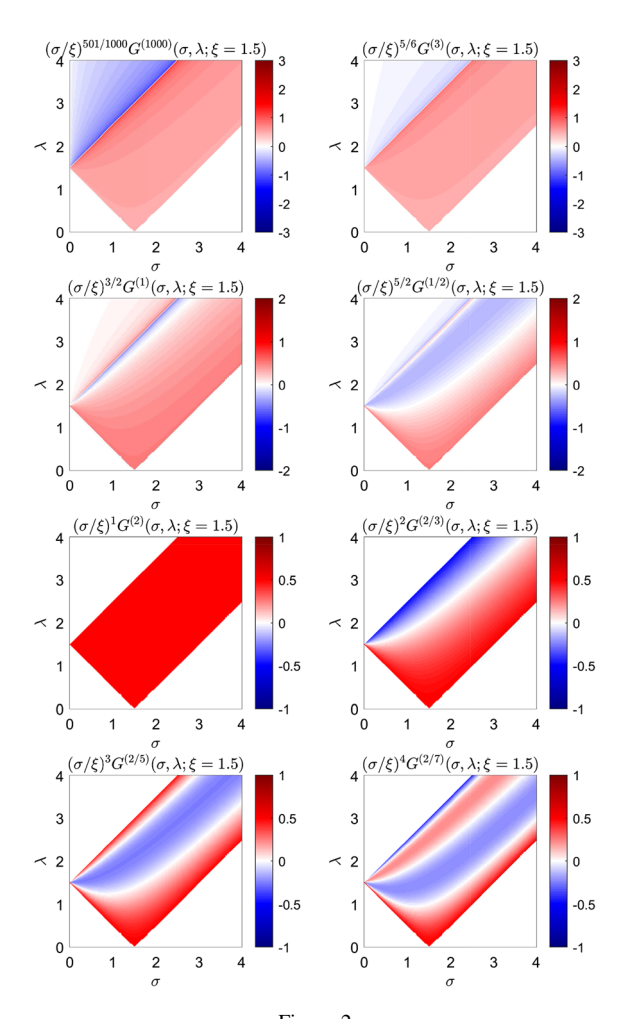


Figure 2 Green's functions with displacement  $\xi=1.5$ ; upper four plots correspond to bay-shapes with  $m\in\{1000,3,1,1/2\}$ , while the lower four plots are related to  $m\in\{2,2/3,2/5,2/7\}$ . A multiplicative factor  $(\sigma/\xi)^{1/2+1/m}$  is included to permit visualization of the far-field behavior. The first four values of m, nonzero values exist for the post-reflection region  $\lambda>\sigma+\xi$ , while for the last four values of m, the expression for  $G^{(m)}$  simplifies, i.e. the Legendre functions become polynomials, and the field in the post-reflection region vanishes. The m=2 Green's function is taking on an especially simple analytical form

This appears to be the general solution form for the equation if m=2, reminiscent of d'Alembert's solution to the wave equation. It is extremely versatile in that it solves the runup problem for a very broad class of initial conditions. Clearly, the solution is immediate and exact for arbitrary  $p(\xi)$  and  $f(\xi)$ , but analytically limited to functions whose product

with  $\xi$  admits an antiderivative. Similarly, the family of functions  $u_0(\sigma)$  for which  $p(\xi)$  is analytically determinable in also restricted to those that have explicit antiderivatives.

The result (14) agrees with the general finding of Didenkulova and Pelinovsky that solutions  $\Phi(\sigma,\lambda)$  in parabolic bays take the form  $\sigma^{-1}[g(\lambda+\sigma)-g(\lambda-\sigma)];$  here our g(z) is the function  $g(z)=zp(|z|)/2+\int\limits_A^{|z|}f(\xi)\xi d\xi/2$  for some arbitrary A satisfying  $|\sigma-\lambda|< A<\sigma+\lambda$ .

For the 2/3-power bays, k = 1,  $P_1(x) = x$  and  $P_1'(x) = 1$ . After simplifications, the potential (13) reduces to

$$\begin{split} \varPhi(\sigma,\lambda) = & \frac{1}{4\sigma^3} \int_{|\sigma-\lambda|}^{\sigma+\lambda} f(\xi) \xi \left(\sigma^2 + \xi^2 - \lambda^2\right) d\xi \\ & - \frac{\lambda}{2\sigma^3} \int_{|\sigma-\lambda|}^{\sigma+\lambda} p(\xi) \xi d\xi \\ & + \frac{1}{2} \left(\frac{\sigma+\lambda}{\sigma}\right)^2 p(\sigma+\lambda) \\ & + \frac{1}{2} \left(\frac{\sigma-\lambda}{\sigma}\right)^2 p(|\sigma-\lambda|). \end{split}$$

The above is generalization of the analytical expression by Garashin et al. (2016) for the case of nonzero velocity in the  $(\sigma, \lambda)$  coordinates.

# 5. Properties and Runup Characteristics of Specific Solutions

Taking into account the general discussion of the previous section, we proceed to analyze runup behavior for specific initial wave profiles.

# 5.1. Definition of the Initial Water Level and Velocity

Recalling our definitions  $p(\sigma) = \Phi(\sigma, 0)$  and  $f(\sigma) = \Phi_{\lambda}(\sigma, 0)$  we pose the initial value problem on the hodograph plane using  $\eta_0(\sigma)$  and  $u_0(\sigma)$  as follows. We approximate the initial velocity in the canal according to Didenkulova and Pelinovsky (2016):

$$u = 2\sqrt{\frac{m+1}{m}} \left(\sqrt{g(h+\eta)} - \sqrt{gh}\right) \approx \sqrt{\frac{m+1}{m}} \sqrt{\frac{g}{h}} \eta. \tag{15}$$

While assuming that the wave height  $\eta \ll h$ , the relationship between x and  $\sigma$  given by (4) simplifies and then

$$h = -\alpha x \approx \frac{1}{4g} \frac{m}{m+1} \sigma^2.$$

Finally, using (4), we derive

$$\Phi_{\sigma}(\sigma,0) = \frac{m}{m+1} u\sigma \approx 2g\eta, \quad \Phi_{\lambda}(\sigma,0) \approx 2g\eta.$$

We now consider a special case of the initial conditions, for which (13) is analytically computable. In particular, we assume a superposition of Gaussian initial displacements:

$$\eta_0(\sigma) = \sum_{i=1}^n a_i e^{-\gamma_j^2 (\sigma - \sigma_{0j})^2}.$$
 (16)

This summation is reducible to the forms chosen for the leading-depression *N*-wave, leading-elevation *N*-wave, and negative Gaussian initial profiles similar to those chosen in Carrier et al. (2003). A single Gaussian and leading depression N-wave profiles under consideration are shown in Fig. 3. In case of (16), we compute

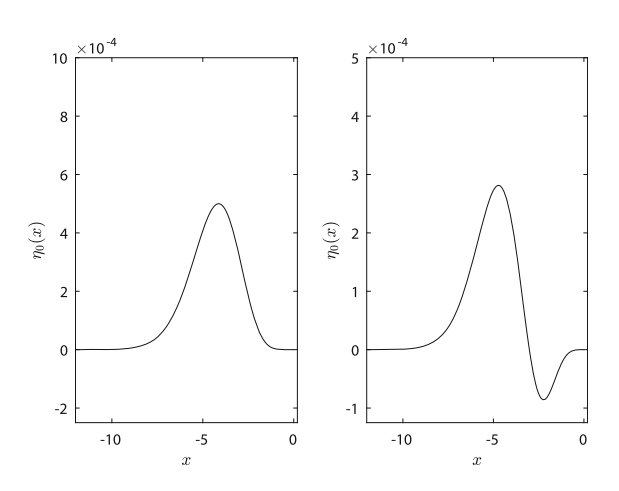


Figure 3 Initial wave profiles associated with the Gaussian (left) and leading depression N-wave (right) in the physical coordinates. Casting from the  $(\sigma,\lambda)$  plane to the physical coordinates is performed using the linearized hodograph transform

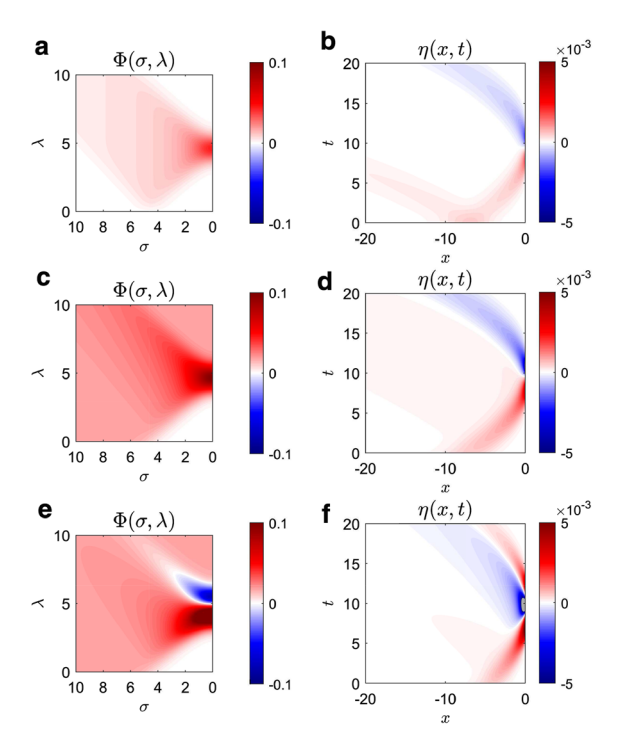


Figure 4
Computed potential  $\Phi$  (left) and water level  $\eta$  (right) in the case of the parabolic bay (m=2). Plots  $\bf a$  and  $\bf b$  are related to the Gaussian wave with zero initial velocity, plots  $\bf c$  and  $\bf d$  are associated with the runup of the Gaussian wave with the nonzero initial velocity, and finally plots  $\bf c$  and  $\bf d$  depict runup of the leading depression N-wave. Detailed views of the water level and velocity near the shoreline are shown in Fig. 5

$$p(\xi) = \int_0^{\xi} \Phi_{\sigma}(\sigma, 0) d\sigma \approx g \sum_{j=1}^n a_j \frac{\sqrt{\pi}}{\gamma_j}$$
$$\left[ \operatorname{erf} \left( \gamma_j (\xi - \sigma_{0j}) \right) + \operatorname{erf} \left( \gamma_j \sigma_{0j} \right) \right],$$
$$f(\xi) \approx 2g \sum_{j=1}^n a_j e^{-\gamma_j^2 (\xi - \sigma_{0j})^2}.$$

Analytical expressions for  $\Phi$ ,  $\Phi_{\sigma}$  and  $\Phi_{\lambda}$  could be then derived for the above realisations of  $p(\xi)$  and  $f(\xi)$ , while taking into the account derivations by Ng and Geller (1969).

#### 5.2. Numerical Experiments

As an example, we consider runup of a single Gaussian with the specific numerical values g = 9.8,  $a_1 = 1/2 \cdot 10^{-3}$ ,  $\gamma_1 = 1$ , and  $\sigma_{01} = 4.5$  on the parabolic and 2/3-power bays. The function  $\Phi$  and its

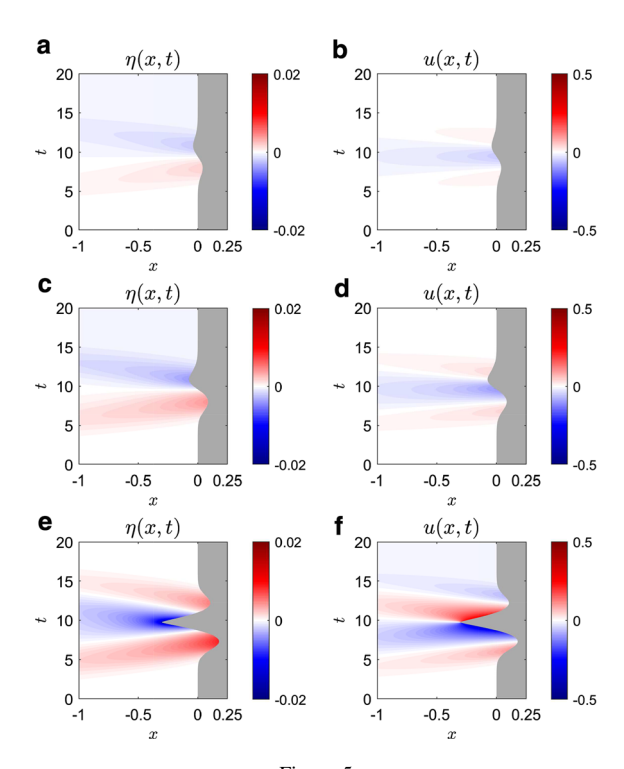


Figure 5
Computed potential  $\eta$  (left) and water level u (right) in the case of the parabolic bay (m=2). Gray area is associated with the dray land. Plots **a** and **b** are related to the Gaussian wave with zero initial velocity, plots **c** and **d** are associated with the runup of the Gaussian wave with the nonzero initial velocity, and finally plots **e** and **f** depict runup of the leading depression N-wave

derivatives are computed analytically using the Symbolic Toolkit in (MATLAB, 2011), and then numerically evaluated on the uniform grid  $(\sigma, \lambda)$ . The contours of  $\Phi(\sigma, \lambda)$  are shown in the left panels of Fig. 4. This is an exact analytic solution on the whole quadrant  $(\sigma \geq 0, \lambda \geq 0)$ ; we do not need to resort to numerical or even semi-analytic methods. The solution in (x, t) coordinates are obtained by solving (4) using the Newton-Raphson method to an arbitrary level of accuracy. We note that in order to compute a Jacobian matrix in the Newton-Raphson method, the derivatives  $x_{\sigma}, x_{\lambda}, t_{\sigma}$ , and  $t_{\lambda}$  are found analytically using the Symbolic Toolkit and then evaluated numerically. Plots of the water level  $\eta(x,t)$  are shown on the right side of Fig. 4.

The first row demonstrates results for the initial water disturbance with a zero water velocity, i.e.  $p(\xi) = 0$ . Note that the initial wave propagates in both directions, as could be easily noted in the graphs

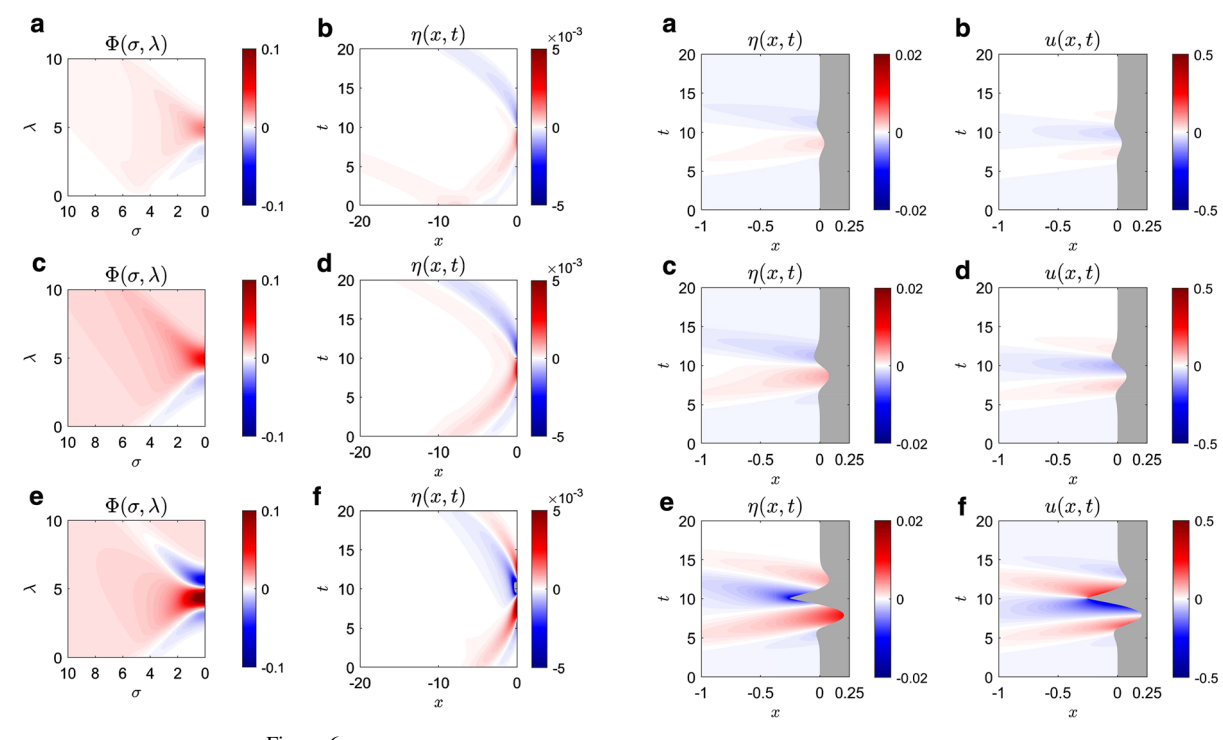


Figure 6 Computed potential  $\Phi$  (left) and water level  $\eta$  (right) in the case of the 2/3-power bay (m=2/3). Plots  $\bf a$  and  $\bf b$  are related to the Gaussian wave with zero initial velocity, plots  $\bf c$  and  $\bf d$  are associated with the runup of the Gaussian wave with the nonzero initial velocity, and finally plots  $\bf e$  and  $\bf f$  depict runup of the leading depression N-wave. Detailed views of the water level and velocity near the shoreline are shown in Fig. 7

Figure 7
Computed potential  $\eta$  (left) and water level u (right) in the case of the 2/3-power bay (m=2/3). Gray area is associated with the dray land. Plots **a** and **b** are related to the Gaussian wave with zero initial velocity, plots **c** and **d** are associated with the runup of the Gaussian wave with the nonzero initial velocity, and finally plots **e** and **f** depict runup of the leading depression N-wave

of  $\eta(x,t)$ , see Fig. 4b. The second and third row of plots are related to scenarios, in which we assume that the initial velocity is given according to (15). Hence, the initial displacement propagates towards the shore and then reflects from it. Finally, the third row shows runup of the leading depression wave. Unlike a single, nearly symmetrical runup, as exhibited for the Gaussian wave, the leading depression wave has a secondary runup and a great drawdown.

Figure 5 display detailed views of the water level and velocity dynamics near the shore. Similarly, the first row is associated with the case of a zero initial velocity. Results in the second and third rows are computed using the water velocity specified according to (15). A reader is prompted to examine shore line dynamics; the gray area is related to the dry land. Comparing the first and second rows, we notice that

inclusion of the initial water velocity increases the runup and water velocity at the shore line. The last row is again associated with the leading depression wave.

Similarly we compare runup of the leading depression N-wave in the parabolic and 2/3-power bays. To construct the N-wave we add a leading depression to the existing Gaussian wave. The depression is parameterized by  $a_2 = -1/3 \cdot 10^{-3}$ ,  $\gamma_2 = 1$ , and  $\sigma_{02} = 4$ . The resultant profile describes a surface displacement on the subduction thrust fault (Carrier et al., 2003). Figure 6 shows the computed potential  $\Phi(\sigma, \lambda)$  and water level  $\eta(x, t)$ . Similar to the Gaussian wave, we note that when the initial velocity is absent, the wave starts to propagate in both directions from the beginning, see Fig. 6b. But unlike in the case of the Gaussian wave, the leading

H. Hartle et al. Pure Appl. Geophys.

Table 1

Initial waves and extreme values of runup and drawdown

	Gaussian wave		N-wave	
$a_1$	$0.5 \cdot 10^{-3}$		$0.5 \cdot 10^{-3}$	
γ1	1		1	
$\sigma_{01}$	4.5		4.5	
$a_2$			$-0.33 \cdot 10^{-3}$	
$\gamma_2$			1	
$\sigma_{02}$			4	
Maximum initial displacement	$5.0 \cdot 10^{-4}$		$2.8 \cdot 10^{-4}$	
Parabolic bay, $m = 2$	$u_0 = 0$	$u_0 = \sqrt{\frac{m+1}{m} \frac{g}{h}} \eta$	$u_0 = 0$	$u_0 = \sqrt{\frac{m+1}{m} \frac{g}{h}} \eta$
Maximum runup	$1.98 \cdot 10^{-3}$	$4.32 \cdot 10^{-3}$	$1.82 \cdot 10^{-3}$	$3.79 \cdot 10^{-3}$
Maximum drawdown	$-1.97 \cdot 10^{-3}$	$-3.69 \cdot 10^{-3}$	$-1.29 \cdot 10^{-3}$	$-2.44 \cdot 10^{-3}$
Maximum shoreward velocity	$2.05 \cdot 10^{-2}$	$4.43 \cdot 10^{-2}$	$2.82 \cdot 10^{-2}$	$5.88 \cdot 10^{-2}$
Maximum offshore velocity	$-4.57 \cdot 10^{-2}$	$-9.24 \cdot 10^{-2}$	$-3.98 \cdot 10^{-2}$	$-7.95 \cdot 10^{-2}$
2/3-power bay, $m = 2/3$	$u_0 = 0$	$u_0 = \sqrt{\frac{m+1}{m} \frac{g}{h}} \eta$	$u_0 = 0$	$u_0 = \sqrt{\frac{m+1}{m} \frac{g}{h}} \eta$
Maximum runup	$3.85 \cdot 10^{-3}$	$8.95 \cdot 10^{-3}$	$4.68 \cdot 10^{-3}$	1.02·10 <sup>-2</sup>
Maximum drawdown	$-7.57 \cdot 10^{-3}$	$-1.51 \cdot 10^{-3}$	$-6.43 \cdot 10^{-3}$	$-1.27 \cdot 10^{-2}$
Maximum shoreward velocity	$1.42 \cdot 10^{-1}$	$2.76 \cdot 10^{-1}$	$1.22 \cdot 10^{-1}$	$2.37 \cdot 10^{-3}$
Maximum offshore velocity	$-1.54 \cdot 10^{-1}$	$-3.24 \cdot 10^{-1}$	$-1.65 \cdot 10^{-1}$	$-3.39 \cdot 10^{-3}$

depression is now clearly distinguishable in the  $\eta(x,t)$  plots. Detailed view of the water level and velocity are shown in Fig. 7. The maximum runup as in the previous simulation is twice greater, when the initial water level is prescribed. Values of the maximum runup and drawdown for all cases are listed in Table 1. For the 2/3-power bay, the runup and drawdown are significantly increased if compared to those occurring in the parabolic bay. Furthermore, the 2/3-power bay again has an additional runup event, which is a signature of this geometry.

We note that there are strong similarities between Carrier et al. (2003) and dynamics in the parabolic bay. In the case of the plane beach, they observed a near symmetry of  $\eta(x,t)$  around the peak runup for the Gaussian cases. Similarly, the parabolic bay case has a significant amount of symmetry as well. The symmetry starts to break down for the N-wave initial displacement due to skewness of the initial displacement. The symmetry is somewhat broken for the 2/3-power bay, with the first runup larger than the second one in case of the Gaussian wave.

# 5.3. Comparison with the Finite Difference Solution

In this section, we compare the analytical results to direct numerical integration of (1) using a finite difference method. Similar to Nicolsky et al. (2011), we consider a flux-based implementation of (1):

$$S_t + U_x = 0, \qquad U_t + (uU)_x + gS\eta_x = 0,$$
 (17)

where the flux U = uS and water level  $\eta = H - h$ . In the case of *m*-power bays, the water depth *H* is related to the area *S* according to  $H = (\alpha S)^{1/\alpha}$ . Here,  $\alpha = 1 + 1/m$ .

We approximate the system (17) on a staggered uniform grid by finite differences. The spatial derivatives are discretized by central difference and upwind difference schemes (Fletcher, 1991). We also employ the semi-implicit scheme in time using a first order scheme (Kowalik & Murty, 1993). The runup and rundown algorithm is based on Nicolsky et al. (2011). The finite difference scheme is coded in Matlab, and spatial and temporal time steps are  $\Delta x = 5 \cdot 10^{-3}$  and  $\Delta t = 5 \cdot 10^{-4}$ , respectively. For the initial conditions, we assume a leading depression N-wave, which is cast from the  $(\sigma, \lambda)$  plane to the

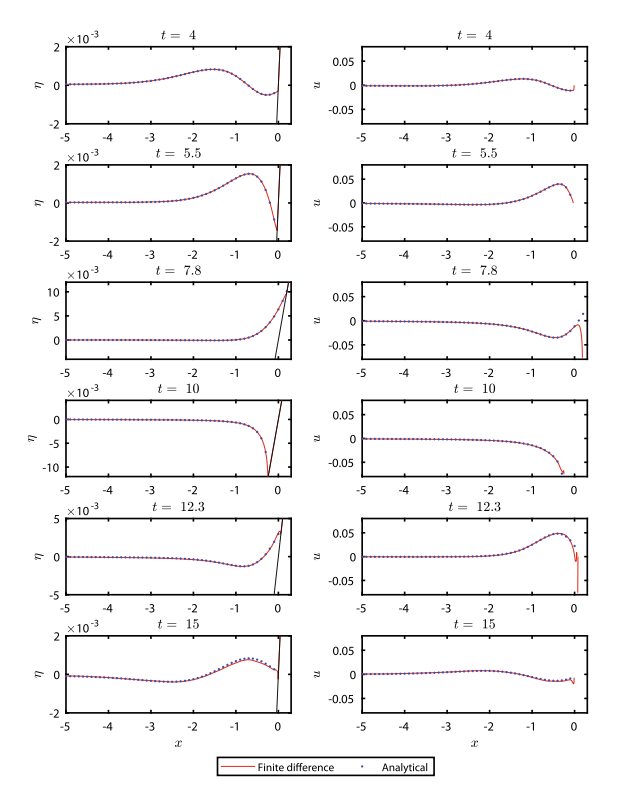


Figure 8 Comparison of the analytically computed and numerically modeled water level  $\eta$  and velocity u at several key moments during runup of the leading depression N-wave in the 2/3-power bay

physical coordinates using the linearized hodograph transform.

Figure 8 shows snapshots of the water level  $\eta$  and velocity u at several key moments during runup of the leading depression N-wave in the 2/3-power bay. In the considered scenario, the initial water velocity is prescribed according to (15). At each snapshot, we compare the analytical solution to its finite difference counterpart, as follows. At t = 4, the wave approaches the head of the bay. The first drawdown occurs at t = 5.5, as the leading depression arrives in full force. Then at t = 7.8 the first runup occurs, followed by another drawdown at t = 10 and runup at t = 12.3. The wave retreats and its shape is then captured at t = 15. We note that in all cases, the analytically computed water level  $\eta$  matches its counterpart very well. Unfortunately, the comparison is not so good for the water velocity near the maximum runup. Recall that the finite difference scheme is based on the flux formulated Eq. (17), and hence the velocity is computed as u = U/S. When S is close to zero, e.g. near the maximum runup, the division U/S is prone to errors.

We emphasize the analytical solution is computed by the Newton-Raphson method and is free of any artifacts. Furthermore, the analytical solution could be computed for any point (x, t) at once, without a need to compute preceding wave dynamics. The number of iterations in the Newton-Raphson method is typically limited to six, before the machine accuracy, e.g.  $10^{-16}$  is obtained, and it takes less than a second to do so, once all derivatives  $x_{\sigma}, x_{\lambda}, t_{\sigma}$ , and  $t_{\lambda}$  are found symbolically.

### 6. Conclusions

We have posed and solved the initial-value problem in *U*-shaped and *V*-shaped bays of infinite length by integration of Green's function. For arbitrary values of m, the Green's function consists of Legendre functions. The latter and its derivatives could be readily computed by hypergeometric functions in MATLAB, leading to evaluation of the potential through a single integral. For 2/(2k+1)power bays, the analytical expressions greatly simplify, resulting in explicit, closed-form solutions for initial displacements described by a sum of Gaussian functions on the hodograph plane. For practical purposes, for assessment of the initial conditions in the physical plane, a linearized hodograph transform could be used for casting a sum of Gaussian waves from the hodograph plane to the physical space. Parameters in Gaussian waves in the hodograph plane could be adjust until a match to the desired wave in the geophysical sense is obtained. Once all analytical expressions for the potential and its derivatives are found, evaluation of the water level and velocity is completed through the hodograph transform using the Newton-Raphson method to an arbitrary degree of accuracy.

#### Acknowledgements

We would like to thank anonymous referees for careful reading of the manuscript and valuable comments, which have been very helpful in improving the manuscript. Alexei Rybkin acknowledges support from National Science Foundation Grant (NSF) award DMS-2009980 and DMS-1716975. Dmitry Nicolsky acknowledges support from the Geophysical Institute, University of Alaska Fairbanks. Efim Pelinovsky acknowledges support by Laboratory of Dynamical Systems and Applications NRU HSE, by the Ministry of science and higher education of the RF Grant ag. 075-15-2019-1931 and by RFBR Grant 20-05-00162. Harry Hartle was supported by the National Science Foundation Research Experience for Undergraduate program (Grant DMS-1716975).

#### **Declarations**

Conflict of Interest The authors have no relevant financial or non-financial interests to disclose. The authors have no conflicts of interest to declare that are relevant to the content of this article.

**Publisher's Note** Springer Nature remains neutral with regard to jurisdictional claims in published maps and institutional affiliations.

# REFERENCES

- Antuono, M., & Brocchini, M. (2007). The boundary value problem for the nonlinear shallow water equations. Studies in Applied Mathematics. 119, 73–93.
- Antuono, M., & Brocchini, M. (2010). Solving the nonlinear shallow-water equations in physical space. *Journal of Fluid Mechanics*, 643, 207–232.
- Aydin, B., & Kânoğlu, U. (2017). New analytical solution for nonlinear shallow water-wave equations. *Pure and Applied Geophysics*, 174, 3209–3218.
- Bernard, E., & Titov, V. (2015). Evolution of tsunami warning systems and products. *Philosophical Transactions of the Royal* Society A, 373, 20140371.
- Carrier, G., & Greenspan, H. (1958). Water waves of finite amplitude on a sloping beach. *Journal of Fluid Mechanics*, 01, 97–109.
- Carrier, G., Wu, T., & Yeh, H. (2003). Tsunami run-up and drawdown on a plane beach. *Journal of Fluid Mechanics*, 475, 79–99.
- Chugunov, V., Fomin, S., Noland, W., & Sagdiev, B. (2020). Tsunami runup on a sloping beach. *Computational and Mathematical Methods*, 2(1), e1081.

- Didenkulova, I. (2009). Applied wave mathematics: Selected topics in solids, fluids, and mathematical methods. In E. Quak & T. Soomere (Eds.), Chap New trends in the analytical theory of long sea wave runup (pp. 265–296). Berlin.
- Didenkulova, I., & Pelinovsky, E. (2009). Non-dispersive traveling aves in inclined shallow water channels. *Physics Letters A*, 373(42), 3883–3887.
- Didenkulova, I., & Pelinovsky, E. (2011a). Nonlinear wave evolution and runup in an inclined channel of parabolic cross-section. *Physics of Fluids*, 23(8), 384–390.
- Didenkulova, I., & Pelinovsky, E. (2016). On shallow water rogue wave formation in strongly in homogenous channels. *Journal of Physicals A*, 49, 194001(11p).
- Didenkulova, I., Pelinovsky, E., & Soomere, T. (2009). Runup characteristics of symmetrical solitary tsunami waves of "unknown" shapes. *Pure and Applied Geophysics*, 165(11–12), 2249–2264.
- Didenkulova, I., Pelinovsky, E., Soomere, T., & Zahibo, N. (2007).
  Tsunami and nonlinear waves. In A. Kundu (Ed.), Chap runup of nonlinear asymmetric waves on a plane beach (pp. 175–190).
  Springer.
- Dobrokhotov, S., Medvedev, S., & Minenkov, D. (2013). On transforms reducing one-dimensional systems of shallow-water to the wave equation with sound speed  $c^2 = x$ . *Mathematical Notes*, 93, 704–714.
- Dobrokhotov, S., Nazaikinskii, V., & Tirozzi, B. (2010). Asymptotic solution of the one-dimensional wave equation with localized initial data and with degenerating velocity. *Russian Journal of Mathematical Physics*, 17, 434–447.
- Dobrokhotov, S., & Tirozzi, B. (2010). Localized solutions of onedimensional non-linear shallow-water equations with velocity  $c = \sqrt{x}$ . Russian Mathematical Surveys, 65(1), 177–179.
- Fletcher, C. (1991). Computational techniques for fluid dynamics 1 (p. 401). Springer-Verlag.
- Garashin, V., Harris, M., Nicolsky, D., Pelinovsky, E., & Rybkin, A. V. (2016). An analytical and numerical study of long wave run-up in U-shaped and V-shaped bays. *Applied Mathematics* and Computation, 297, 187–197.
- Gradshteyn, IS., & Ryzhik, IM. (1996). Table of integrals, series, and products, fifth, revised edn. Academic Press, translated from the Russian, Translation edited and with a preface by Alan Jeffrey
- Harris, M., Nicolsky, D., Pelinovsky, E., Pender, J., Rybkin, A., et al. (2016). Run-up of nonlinear long waves in U-shaped bays of finite length: Analytical theory and numerical computations. *Journal of Ocean Engineering and Marine Energy*, 2, 113–127.
- Johnson, R. (1997). A modern introducquittion to the mathematical theory of water waves (1st ed., p. 464). Cambridge University Press.
- Kânoğlu, U., & Synolakis, C. (2006). Initial value problem solution of nonlinear shallow water-wave equations. *Physical Review Letters*, 148501, 97.
- Kowalik, Z., & Murty, T. (1993). Numerical modeling of ocean dynamics (p. 481). World Scientific.
- Madsen, P., & Fuhrman, D. (2008). Run-up of tsunamis and long waves in terms of surf-similarity. *Coastal Engineering*, 55(3), 209–223.
- Madsen, P., & Schäffer, H. (2010). Analytical solutions for tsunami runup on a plane beach: single waves, N-waves and transient waves. *Journal of Fluid Mechanics*, 645, 27–57.

- MATLAB. (2011). version 7.13.0.564 (R2011b). The MathWorks Inc., Natick, Massachusetts
- Ng, E., & Geller, M. (1969). A table of integrals of the Error functions, Section B.—Mathematical Sciences. *Journal of Research of the National Bureau of Standards*, 73B(1), 20.
- Nicolsky, D., Pelinovsky, E., Raz, A., & Rybkin, A. (2018). General initial value problem for the nonlinear shallow water equations: Runup of long waves on sloping beaches and bays. *Physics Letters A*, 382(38), 2738–2743.
- Nicolsky, D., Suleimani, E., & Hansen, R. (2011). Validation and verification of a numerical model for tsunami propagation and runup. *Pure and Applied Geophysics*, 168, 1199–1222.
- Pedersen, G., & Gjevik, B. (1983). Run-up of solitary waves. *Journal of Fluid Mechanics*, 142, 283–299.
- Pelinovsky, E., & Mazova, R. (1992). Exact analytical solutions of nonlinear problems of tsunami wave run-up on slopes with different profiles. *Natural Hazards*, 6, 227–249.
- Raz, A., Nicolsky, D., Rybkin, A., & Pelinovsky, E. (2018). Long wave runup in asymmetric bays and in fjords with two separate heads. *Journal of Geophysical Research: Oceans*, 123(3), 2066–2080.
- Rybkin, A. (2019). Method for solving hyperbolic systems with initial data on non-characteristic manifolds with applications to the shallow water wave equations. *Applied Mathematics Letters*, 93, 72–78.
- Rybkin, A., Nicolsky, D., Pelinovsky, E., & Buckel, M. (2021). The generalized Carrier-Greenspan transform for the shallow

- water system with arbitrary initial and boundary conditions. Water Waves, 3(1), 267–296.
- Rybkin, A., Pelinovsky, E., & Didenkulova, I. (2014). Nonlinear wave run-up in bays of arbitrary cross-section: Generalization of the Carrier-Greenspan approach. *Journal of Fluid Mechanics*, 748, 416–432.
- Shimozono, T. (2016). Long wave propagation and run-up in converging bays. *Journal of Fluid Mechanics*, 798, 457–484.
- Shimozono, T. (2020). Kernel representation of long-wave dynamics on a uniform slope. *Proceedings of the Royal Society* A, 476, 20200333.
- Shimozono, T. (2021). Tsunami propagation kernel and its applications. *Natural Hazards and Earth System Sciences Discussions*, 2021, 1–21.
- Stoker, J. (1957). Water waves: The mathematical theory with applications (p. 567). Interscience Publishers.
- Synolakis, C. (1991). Tsunami runup on steep slopes: How good linear theory really is? *Natural Hazards*, 4, 221–234.
- Synolakis, C., & Deb, M. (1988). On the anomalous behavior of the runup of cnoidal waves. *Physics of Fluids*, 31, 1–4.
- Tinti, S., & Tonini, R. (2005). Analytical evolution of tsunamis induced by near-shore earthquakes on a constant-slope ocean. *Journal of Fluid Mechanics*, *535*, 33–64.
- Zahibo, N., Pelinovsky, E., Golinko, V., & Osipenko, N. (2006).
  Tsunami wave runup on coasts of narrow bays. *International Journal of Fluid Mechanics Research*, 33, 106–118.

(Received March 26, 2021, revised September 3, 2021, accepted September 28, 2021)